

# Full-field-of-view aberration correction for large arrays of focused beams

Y. Machu,<sup>1</sup> G. Creutzer,<sup>1</sup> C. Sayrin,<sup>1,2</sup> and M. Brune<sup>1,\*</sup>

<sup>1</sup>*Laboratoire Kastler Brossel, Collège de France, CNRS, ENS-Université PSL,  
Sorbonne Université, 11 place Marcelin Berthelot, F-75231 Paris, France*

<sup>2</sup>*Institut Universitaire de France, 1 rue Descartes, 75231 Paris Cedex 05, France*

(Dated: December 19, 2025)

We propose and implement an aberration correction method for the creation of extended arrays of spots well beyond the isoplanatic region of any optical system. The method relies on an extensive calibration of aberrations in terms of Zernike polynomials over the full accessible field of an optical system. We introduce a modified Gerchberg-Saxton algorithm for generating holographic phase masks creating fully corrected arbitrary arrays of spots. By applying the method to an aspherical lens, and using a liquid-crystal spatial light modulator (SLM), we increase the aberration-free field of view from 50 to 500  $\mu\text{m}$ , only limited by the largest diffraction angles accessible to the SLM. This opens new perspectives for the generation of large arrays of optical tweezers, especially for neutral atom based quantum processors and simulators.

## I. INTRODUCTION

Control of optical aberrations plays an essential role in designing optical systems to reach diffraction-limited performances[1]. It is of paramount importance for large-field-of-view imaging with high-numerical-aperture lenses[2, 3] and to create arrays of optical tweezers, with applications in biology[4–8], parallel laser micromachining[9–14] and micromanipulation[8, 15, 16], parallel 3D printing[17–19] and trapping of single atoms[20–23], with recent developments that led to the creation of large arrays of tweezers trapping thousands of atoms[24–27]. A single lens can be used to reach the diffraction limit on its optical axis even with a large numerical aperture by using an aspherical surface that suppresses the spherical aberration. However, this simple system has a limited field of view (FOV) due to growing aberrations away from the optical axis. A standard solution consists in combining many lenses whose individual aberrations cancel each other in optimized combinations. Nevertheless, these assemblies, which often contain ten to twenty lenses, are complex, bulky and expensive.

Beyond design optimization, adaptive optics[2, 28–31] has become a popular method of aberration compensation. It relies on the measurement of the wavefront distortion and on a feed-back correction by a spatial light modulator, such as a deforming mirror or an array of liquid crystals (SLM). This technique enables perfect compensation of geometrical aberrations and the creation of a diffraction-limited spot centered on any given point within the accessible field of view (FOV) of an optical system. However, the spatial dependency of the aberrations limits the efficiency of this method to a restricted isoplanatic area of the order of the native diffraction-limited FOV of the optical system[32–34]. Therefore, local corrections considerably increase the usable FOV but they do not enable the production of an aberration-free image

over the whole accessible field. In the case of aberrations originating from propagation before entering the optical system, e.g. in the atmosphere for astrophysics, this limitation can be overcome using a multiconjugate adaptive optics method significantly increasing the diffraction limited field of view[35]. To the best of our knowledge however, for aberrations introduced by the optical system itself, there is no known adaptive optics solution to correct simultaneously the full accessible optical field.

In this paper, we address the problem of creating an arbitrary array of diffraction-limited spots in the focal plane of an optical system. We propose a new method based on SLM-controlled holography, that corrects simultaneously the aberrations for all the spots in arrays covering the full accessible FOV[36, 37]. We introduce generalized Seidel coefficients as a variant of the well-known Seidel expansion describing the field dependency of the wavefront distortion. Our aberration compensation method relies on a preliminary measurement of only a few generalized Seidel coefficients. As a demonstration, we apply the method to the correction of a standard, aspherical lens with a native FOV limited to  $50 \times 50 \mu\text{m}$ . After correction, we generate large, diffraction-limited arrays of up to 5194 spots in a field of  $500 \times 500 \mu\text{m}$ , only limited by the maximum diffraction angle of our SLM. We fully characterize the optical quality of the spots and we demonstrate a tenfold increase of the size of the diffraction-limited field of view.

## II. PRINCIPLE OF THE METHOD

The principle of our SLM-based optical setup is depicted on fig. 1. A lens **L** of focal length  $f$  creates in its focal plane an array of focused beams with a possibly complex intensity pattern (Bottle beams[39, 40] or Laguerre-Gaussian beams for instance). The SLM[41] is a liquid crystal (LCoS) matrix used as a phase-only modulator. It applies an arbitrary phase mask  $\phi(\rho)$  on the incident wave (wave number  $k$ ). A 4f telescope generates in the back focal plane of **L** an optical field of amplitude

\* Corresponding author: michel.brune@lkb.ens.fr

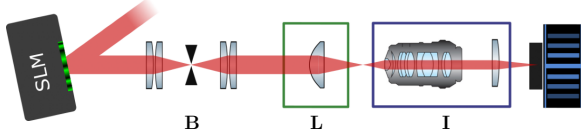


Figure 1. Experimental setup. A collimated input laser beam is diffracted using the SLM. We form the image of the SLM on the back focal plane of the convergent optical system of interest **L** (focal distance  $f$ ) by using an afocal telescope in the 4f configuration. A blade **B** removes the zero-order reflection. An array of spots is formed in the focal plane of **L**. We test the quality of this array by imaging with a camera using an aberration-free optical system **I**[38].

$E(\rho) = \sqrt{I(\rho)} e^{i\phi(\rho)}$  where  $\rho$  is the position coordinate in this plane, with the origin set on the optical axis of **L** and  $I(\rho)$  is the intensity profile of the beam. In the focal plane of an ideal lens, the field amplitude  $F(\mathbf{r})$  is the Fourier transform of  $E(\rho)$ . The origin of coordinate  $\mathbf{r}$  is set on the optical axis of **L**, too.

For the generation of an array of  $N$  spots at positions  $\{\mathbf{r}_p\}_{p \in \{1, \dots, N\}}$  in the focal plane of **L**, the theoretical field amplitude in the back focal plane of an ideal lens reads

$$E_{\text{th}}(\rho) = \sqrt{I(\rho)} a_{\text{th}}(\rho), \quad (1)$$

where  $a_{\text{th}}(\rho) = \sum_p w_p e^{i\frac{k}{f} \mathbf{r}_p \cdot \rho}$  is a superposition of plane waves and  $\{w_p\}$  are complex weights. This amplitude generates an array of spots with an intensity proportional to  $|w_p|^2$ . The shape of individual spots is determined by  $I(\rho)$ , which is supposed to have a slow variation at the scale of the pupil defined by the SLM. As the dimensionless amplitude  $a_{\text{th}}(\rho)$  does not have a uniform modulus, it cannot be generated with a phase-only modulator. One usually uses an iterative Weighted Gerchberg-Saxton (WGS) algorithm[21, 22, 42, 43] to compute a phase mask, that approximately generates the target array of spots. The algorithm uses the following ansatz for the phase  $\phi_{\text{nc}}(\rho)$  of the non-corrected field amplitude in the plane of **L**

$$\phi_{\text{nc}}(\rho) = \arg \left( \sum_p w_p \cdot e^{i\frac{k}{f} \mathbf{r}_p \cdot \rho} \right), \quad (2)$$

which is the phase at position  $\rho$  of the ideal amplitude  $a_{\text{th}}(\rho)$ . The algorithm iterates between the back focal plane and the Fourier plane of an ideal lens by direct and inverse Fourier transforms. It finds complex amplitudes  $w_p$ 's that make the diffraction pattern of  $E_{\text{nc}}(\rho) = \sqrt{I(\rho)} e^{i\phi_{\text{nc}}(\rho)}$  close to that of  $E_{\text{th}}(\rho)$ .

In practice, the lens **L** introduces aberrations, which are not taken into account by the simple Fourier transform used in a standard WGS algorithm. The approximate non-corrected phase mask  $\phi_{\text{nc}}(\rho)$  thus produces arrays of deformed spots whose shape depends on their position in the FOV.

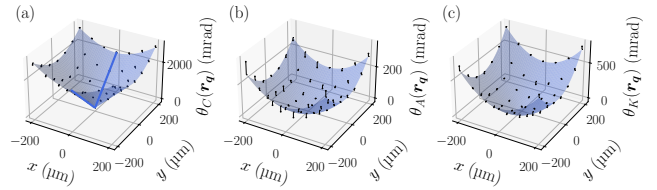


Figure 2. Spatial dependence of the aberrations. (a) First-order coma. The blue line highlights the linear dependence of  $\theta_C(\mathbf{r})$  as a function of  $|\mathbf{r}|$ . Panel (b) corresponds to astigmatism and (c) to curvature. The points are measurement results, while the shaded surfaces correspond to the fits. The drop lines are the residuals of the fits. The paraboloids corresponding to astigmatism and curvature are centered at positions  $(-2\mu\text{m}, -3\mu\text{m})$  and  $(7\mu\text{m}, -18\mu\text{m})$ , respectively. These values are small compared to the dimension of the corrected field. The larger values obtained for the field curvature can be explained by a small tilt between the focal plane of the aspherical lens and the the plane of the camera sensor.

#### Field-dependent aberration correction method.

Let us first consider a single-spot target image at position  $\mathbf{r}_p$  corresponding to the input amplitude  $E_p(\rho) = \sqrt{I(\rho)} e^{i\frac{k}{f} \mathbf{r}_p \cdot \rho}$ . The aberrations introduced by the non-ideal system **L** can be represented by a phase distortion mask  $\Phi(\mathbf{r}_p, \rho)$  producing the amplitude  $E'_p(\rho) = E_p(\rho) e^{i\Phi(\mathbf{r}_p, \rho)}$  when applied to the incident plane wave. When focused by an ideal, i.e., aberration-free lens, this amplitude produces a spot at position  $\mathbf{r}_p$  with the same aberrations as those of the actual lens. The corresponding amplitude in the focal plane is the Fourier transform of  $E'_p(\rho)$  instead of that of  $E_p(\rho)$ . For an arbitrary input amplitude  $E(\rho)$  the amplitude  $F(\mathbf{r})$  in the focal plane of **L**, including the effect of aberrations, is

$$F(\mathbf{r}) = \iint e^{-i\frac{k}{f} \mathbf{r} \cdot \rho} \left\{ E(\rho) e^{i\Phi(\mathbf{r}, \rho)} \right\} d^2 \rho. \quad (3)$$

The function  $\Phi(\mathbf{r}, \rho)$  represents a complete description of geometrical aberrations in the full optical field of **L**. Note that due to the  $\mathbf{r}$  dependency of  $\Phi(\mathbf{r}, \rho)$  equ. (3) is not a Fourier transform.

The adaptive optics correction approach[2, 31] consists in applying with the SLM the phase mask  $-\Phi(\mathbf{r}_p, \rho)$  to the amplitude  $E_p(\rho)$  in order to compensate exactly the aberrations of an image centered at  $\mathbf{r}_p$ . The variation of  $\Phi(\mathbf{r}, \rho)$  as a function of  $\mathbf{r}$  defines the diffraction-limited field of view of **L**. It is usually restricted to the vicinity of the corrected position  $\mathbf{r}_p$ . For this position, the phase-distortion mask  $\Phi(\mathbf{r}_p, \rho)$  can be measured as a function of  $\rho$  by using a phase reconstruction method based on the Gerchberg-Saxton algorithm[21, 38, 44]. In the following, we assume that a mask  $\phi_0(\rho)$  exactly compensating aberrations at  $\mathbf{r} = 0$  has been measured and applied with the SLM in order to cancel aberrations locally, close to the optical axis of the lens. The residual field-dependent aberration of this on-axis pre-compensated system are thus described by  $\Phi(\mathbf{r}, \rho)$  with  $\Phi(0, \rho) = 0$ .

We now present our method for the full-field correction of the off-axis aberrations. It first consists in slightly modifying the WGS ansatz using

$$\phi_c(\rho) = \arg \left( \sum_p w_p e^{i \frac{k}{f} \mathbf{r}_p \cdot \rho} e^{-i \Phi(\mathbf{r}_p, \rho)} \right). \quad (4)$$

in place of  $\phi_{nc}(\rho)$ . The corrected ansatz amounts to applying to each  $\mathbf{k}_p$  component of the sum a phase mask undoing the aberrations that will be introduced by  $\mathbf{L}$ . We then introduce a corrected WGS algorithm[38] where we additionally account for aberrations in the calculation of the field amplitude in the Fourier plane of  $\mathbf{L}$  according to equ. (3). In this way, we can generate phase masks correcting all the spots of an array in a large FOV. The CWGS algorithm has similar convergence as the standard WGS one. To the best of our knowledge, this CWGS was first introduced in[36, 37].

The application of our correction method relies on a precise determination of  $\Phi(\mathbf{r}, \rho)$ . A first approach consists in determining this function sequentially by successively applying with the SLM the phase gradient generating one spot at  $\mathbf{r}_p$ . For this single spot,  $\Phi(\mathbf{r}_p, \rho)$  can be determined with the same phase reconstruction method [44] as used for the determination of  $\phi_0(\rho)$ . However, the determination of  $\Phi(\mathbf{r}, \rho)$  at every spot of the final image is time-consuming, and becomes impractical for the generation of large arrays. Alternatively, we will now show that one can use a simple model of the variations of  $\Phi(\mathbf{r}, \rho)$  as a function of  $\mathbf{r}$  involving only a few parameters, which, once measured, can be used to generate arbitrary corrected arrays without the need of additional measurements.

**Simple model of  $\Phi(\mathbf{r}, \rho)$ .** Following the approach introduced by Seidel to describe the field-dependent aberrations of a centered optical system, we start by a Taylor expansion of  $\Phi(\mathbf{r}, \rho)$  as a function of  $\mathbf{r}$  and  $\rho$ [1]. Due to axial symmetry, all terms with odd global polynomial order in  $\mathbf{r}$  and  $\rho$  vanish. We rewrite the Taylor expansion in terms of Zernike polynomials  $Z_n^m(\rho)$ , with  $n \in \mathbb{N}$ ,  $m \in \mathbb{Z}$  and  $|m| \leq n$ [45, 46]. To the lowest-order terms relevant to describe aberrations, this expansion can be written in terms of the modified Seidel coefficients  $C'$ ,  $A'$ ,  $K'$  and  $D'$ :

$$\begin{aligned} \Phi(\mathbf{r}, \rho) = & C' [x Z_3^1(\rho) + y Z_3^{-1}(\rho)] \\ & + A' [(x^2 - y^2) Z_2^2(\rho) + 2xy Z_2^{-2}(\rho)] \\ & + K' (x^2 + y^2) Z_2^0(\rho) \\ & + D' [(x^2 + y^2)x Z_1^1(\rho) + (x^2 + y^2)y Z_1^{-1}(\rho)] + \dots \end{aligned} \quad (5)$$

where  $x$  and  $y$  are the cartesian components of  $\mathbf{r}$ . The modified Seidel coefficients  $C'$ ,  $A'$ ,  $K'$  and  $D'$  describe the coma, astigmatism, field curvature and distortion, respectively. As a result of pre-compensation using the phase mask  $\phi_0(\rho)$ , all these aberrations vanish on the optical axis and have a polynomial dependency on  $\mathbf{r}$ .

The modified Seidel coefficients are linear combinations of the standard ones[38]. The former can be more easily measured by the method described below, which benefits from the orthogonality of Zernike polynomials.

### III. EXPERIMENTAL CHARACTERIZATION OF FIELD-DEPENDENT ABERRATIONS

We apply our aberration compensation method to a standard aspherical lens (Asphericon AFL12-15-P-U-285). It is optimized at the wavelength of 285 nm. Its measured Strehl ratio is 0.7 on the optical axis at our working wavelength of 821 nm, with a numerical aperture of 0.37 and a focal length  $f = 16.32$  mm. The imaging system (**I** in fig. 1) is a combination of microscope objectives described in[38]. We have carefully checked that it introduces negligible coma, astigmatism and curvature into the full field. The SLM is illuminated by a Gaussian beam of waist 5.2 mm, and we apply a pupil of 12 mm diameter on the SLM.

To characterize field aberrations, we successively measure the wavefronts  $\phi_q(\rho) = \Phi(\mathbf{r}_q, \rho)$  for single spots located at positions  $\mathbf{r}_q$  of a  $7 \times 7$  square reference array centered on the optical axis. The reference array covers a square field of  $400 \times 400 \mu\text{m}$ . By defining the  $\theta_n^m(\mathbf{r}_q)$  coefficients as the scalar product[38] between  $\phi_q(\rho)$  and the Zernike polynomial  $Z_n^m(\rho)$  we get

$$\phi_q(\rho) = \sum_{n,m} \theta_n^m(\mathbf{r}_q) Z_n^m(\rho). \quad (6)$$

We obtain the coefficients  $C'$ ,  $A'$  and  $K'$  with a fit to the measured values of the corresponding  $\theta_n^m(\mathbf{r}_q)$ , with a linear function of  $\mathbf{r}$  for the coma and quadratic functions of  $\mathbf{r}$  for the astigmatism and curvature. For the quadratic fits of astigmatism and curvature, we also take as free parameters the centers of the paraboloids and take them into account in the correction process[38]. It amounts to introducing odd-order terms in the Taylor expansion of  $\Phi(\mathbf{r}, \rho)$ . This is a heuristic approach, which accounts for imperfect axial symmetry of the setup and improves the quality of the correction. We also measured the distortion coefficient  $D'$  and we show in[38] that it is probably dominated by that of the imaging system. We thus did not consider the distortion term in the correction process.

We show in fig. 2 the variation of the functions  $\theta_X(\mathbf{r}) = \sqrt{\theta_n^m(\mathbf{r})^2 + \theta_{-n}^m(\mathbf{r})^2}$  with  $(X, n, m) = (C, 3, 1)$ ,  $(A, 2, 2)$  and  $(K, 1, 1)$  for coma, astigmatism and curvature, respectively. The linear dependence of the two terms  $\theta_3^{\pm 1}(\mathbf{r})$  contributing to coma translates into a linear variation of  $\theta_C(\mathbf{r})$  as a function of the distance  $|\mathbf{r}|$  to the optical axis (fig. 2(a)). The astigmatism and curvature terms (fig. 2(b-c)) have the expected quadratic dependency with respect to  $|\mathbf{r}|$ . From the linear and quadratic fits, we obtain the values of the modified Seidel coefficients  $C' = 10.04(4) \text{ mrad}/\mu\text{m}$ ,  $A' = 3.30(7) \text{ \mu rad}/\mu\text{m}^2$  and  $K' = 8.30(7) \text{ \mu rad}/\mu\text{m}^2$ . These values are close to

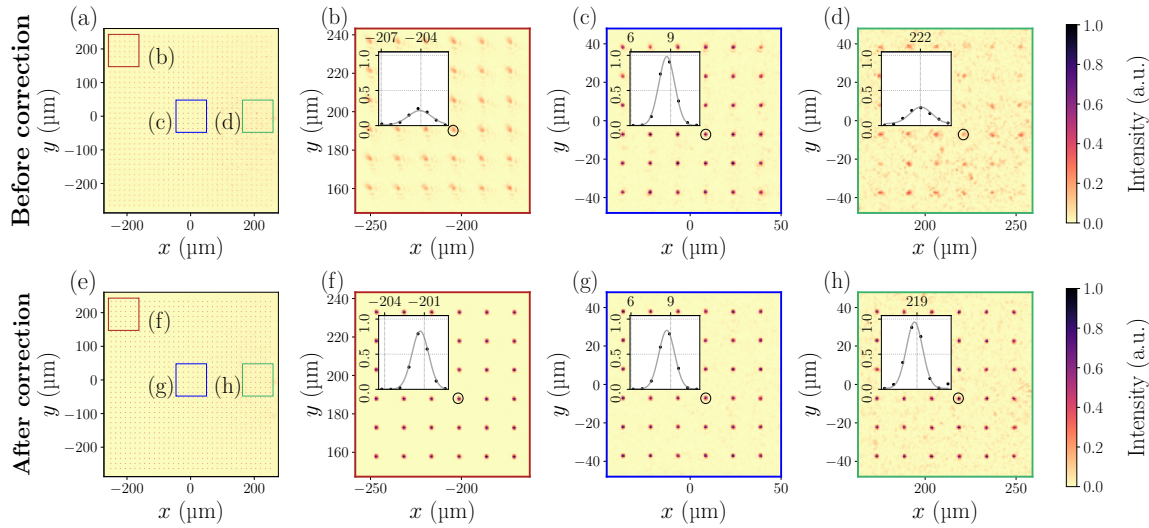


Figure 3. Images of two  $34 \times 34$  arrays without [WGS, panels (a-d)] and with field aberration correction [CWGS, panels (e-h)]. The six right panels are zooms onto regions of interest defined by colored squares on the corresponding left panel. Intensities are normalized to the maximum intensity of the central spot highlighted by a circle on panel (c) and (g). The insets are cross-sections along the  $x$  direction of the intensity profile of the spots highlighted by a black circle in each panel. Cross-sections are centered to contain the highest-intensity pixel of the selected spot.

those calculated from the lens geometry using the OSLO software[47] presented in table S1 (Supplementary material). From the measurements, we also obtain the second-order coma coefficient  $C'' = 0.13(1)$  mrad/ $\mu\text{m}$  and take it into account in the aberration correction[38] (see definition in supplementary material). Note that  $C''$  is two orders of magnitude smaller than  $C'$ , it has a marginal impact on the final quality of the spots. It was not necessary to include more terms to reach the diffraction limit over a large field of view.

#### IV. RESULTS

Using the WGS and CWGS algorithms, we generate two phase masks corresponding to a  $34 \times 34$  square array with a  $d = 15 \mu\text{m}$  step. These arrays contain 1156 spots and cover a  $495 \times 495 \mu\text{m}$  field of view, close to the maximal value of  $535 \mu\text{m}$  corresponding to the Nyquist limit set by the number of pixels of the SLM, the wavelength and the focal length of  $\mathbf{L}$ . The focal plane of the aspherical lens is imaged on the camera using a combination of microscope objectives imaging the full array (see Supplementary Material[38]).

Figure 3(a) shows the full-field image of a non-corrected array generated using the WGS algorithm and including aberration compensation on the optical axis only with the phase mask  $\phi_0(\rho)$ . Figures 3(b-d) are zooms onto various regions depicted by squares on fig. 3(a). The insets are horizontal cross-sections of the spots highlighted by a circle on the corresponding panel. Panel (c) shows diffraction-limited performance for spots located up to  $25 \mu\text{m}$  from the optical axis. This defines

the native field of view of the aspherical lens. Panel (b) shows a strong distortion of spots, mainly due to coma. Panel (d) is close to the zeroth diffraction order of the SLM located at the right border of the array. In addition to aberrations, it shows significant fluctuations of maximal intensities and an important background speckle. Figures 3(e-h) show similar images obtained after full-field aberration compensation based on the CWGS algorithm. The high quality of spots even close to the border of the array is conspicuous. Spots located at the border of the array have similar maximum intensities and shapes as the central spot depicted in the inset of fig. 3(g).

In order to quantitatively assess the performances of the aberration compensation method, we perform individual two-dimensional Gaussian fits of the focal points including a uniform background intensity[38]. We determine for each spot the larger waist  $w_{\max}$ , the ellipticity  $1 - w_{\min}/w_{\max}$  (with  $w_{\min}$  the smaller waist), the orientation of the major axis of the elliptical shape, and the Strehl ratio. The variation of these parameters within the field of view is represented on fig. 4. At the center of the image, the largest waist before correction [fig. 4(a), left panel] is about  $1.2 \mu\text{m}$  on the optical axis, close to the expected diffraction limit estimated at  $1.09(1) \mu\text{m}$  [38]. It increases rapidly to about  $2 \mu\text{m}$  with a broad distribution (green histogram on right panel) when the distance to the optical axis is larger than  $25 \mu\text{m}$ . After field aberration correction, one observes a strong reduction of the largest waist whose distribution (green histogram on right panel) peaks at  $1.19(7) \mu\text{m}$ . The standard deviation of the larger-waist distribution is strongly reduced, too, by the aberration correction, from  $0.5 \mu\text{m}$  to  $0.1 \mu\text{m}$ .

Figure 4(b) presents the ellipticity of the spots. Be-

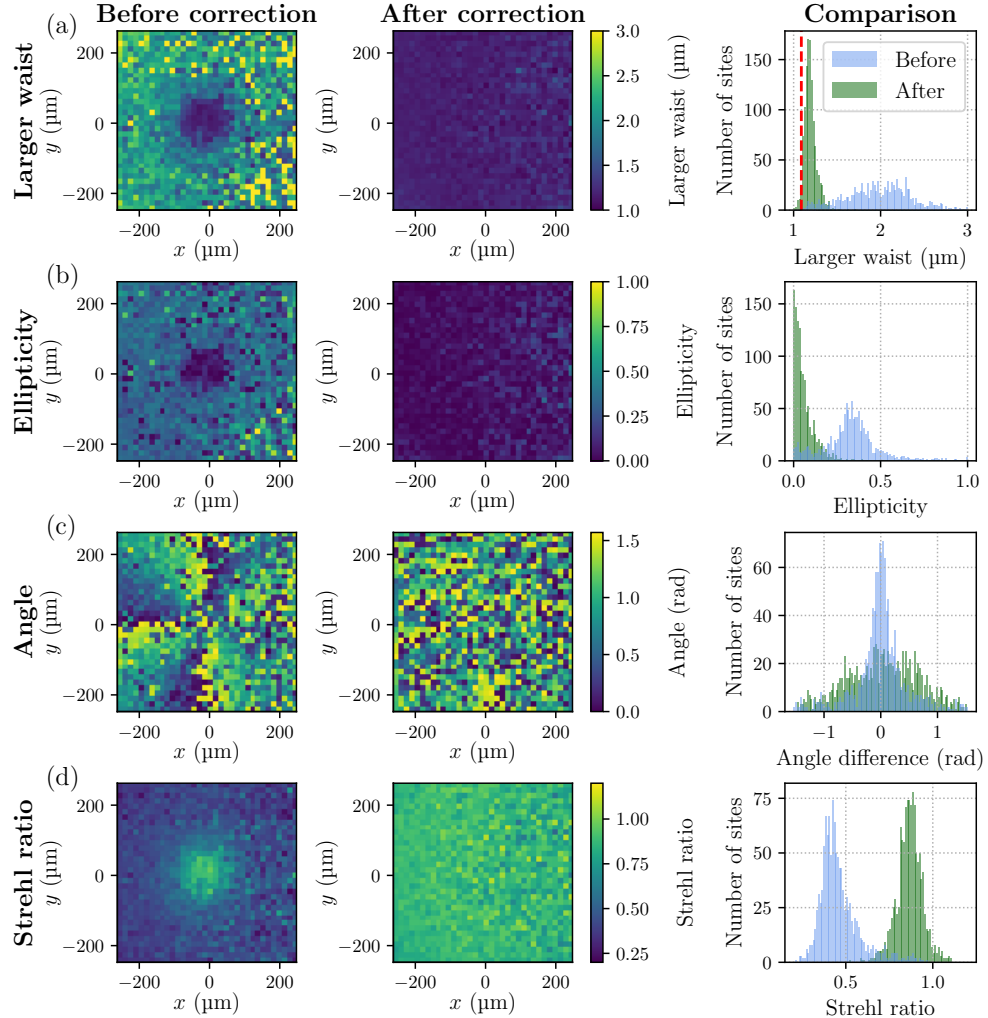


Figure 4. Performance of the aberration correction procedure. (a) Spatial variation of the larger waist of spots, determined by Gaussian fits before (left) and after (center) applying field correction. In both cases, the global correction mask  $\phi_0$  corrects aberrations on the optical axis. Right panel: histogram of larger-waist distribution before (blue) and after correction (green). The vertical dotted line corresponds to the expected diffraction-limited waist. (b-d) Similar representations of the ellipticity (b), of the orientation of the major axis of spots (c) and of the Strehl ratio of the spots (d). For the two left panels of (c) we represent the orientation of the major axis of ellipses relative to the  $x$  axis. The right panel of (c) represents the histogram of the orientation of the major axis of ellipses relative to a radial axis.

fore field correction, most of the spots have an elliptical shape. After field correction, the ellipticity of the spots drops to the negligible average value of 0.07(7), and all spots are nearly circular. Left panel of figure 4(c) shows a clear radial orientation of the major axis of the elliptical spots observed without field correction. After field correction, the orientation of ellipses is dominated by noise [central panel of figure 4(c)], without any structure even at the border of the field. Figure 4(d) presents the spatial

variation of the Strehl ratio,  $S$ . Without field correction, it defines a diffraction-limited field of view ( $S > 0.8$ ) of about  $50 \mu\text{m}$  diameter with an average value over the full-field  $\bar{S} = 0.46$ . After field correction, the average value of the Strehl ratio increases to  $\bar{S} = 0.87(7)$ . One observes a homogeneous performance over the full field of view with a maximal diagonal extension of  $700 \mu\text{m}$ , demonstrating the ability of our method to correct the aberrations simultaneously for all the spots within the full accessible

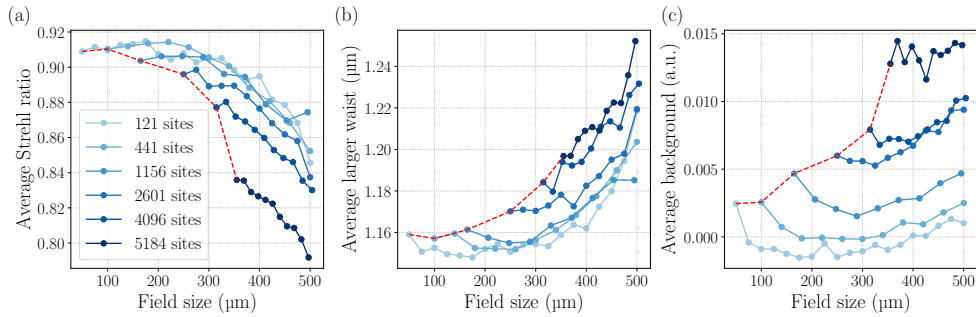


Figure 5. Performance of the aberration correction as a function of the field size for a number of spots ranging from 121 to 5184. Lines connecting data points are a guide to the eyes. For each number of spots the smallest array corresponds to  $d = 5 \mu\text{m}$ . For the largest number of spots  $d$  ranges from 5 to 7  $\mu\text{m}$ . (a), (b) and (c) present the variation of the average value of the Strehl ratio  $\bar{S}$ , maximum waist  $\bar{w}_{\max}$  and background intensity  $\bar{I}_{\text{back}}$  respectively. The latter is normalized to the maximum intensity of the central spot highlighted by a circle on fig. 2(g). A red dotted line connects the datapoints with  $d = 5 \mu\text{m}$ .

optical field.

Finally, we study the quality of the corrected arrays as a function of their spatial extension and spot density for arrays containing from 121 to 5184 spots in a field of view ranging up to 500  $\mu\text{m}$ . For each number of spots the distance  $d$  varies from 5  $\mu\text{m}$  to the maximal value corresponding to an array size of 500  $\mu\text{m}$ . As seen on fig 5(a), the arrays with up to 1156 spots have an average Strehl ratio  $\bar{S}$  above 0.9 for fields up to 300  $\mu\text{m}$ . The corresponding standard deviation of  $\bar{S}$  is  $< 0.1$ . We observe no more than 10% decrease of  $\bar{S}$  for field sizes larger than 300  $\mu\text{m}$ . For the explored range of arrays, the average larger waist [fig 5(b)] only increases by about 10% for the largest array with the highest spot density. The background intensity [fig 5(c)] is not significant[38] up to about 1000 sites in the arrays. It grows significantly for larger arrays when increasing the size of the field. For the largest array, the background intensity integrated over the 5  $\mu\text{m}$  diameter region of interest used for the fit is on average 14% of the total power of the integrated Gaussian peak. The background intensity is related to a speckle background clearly visible on fig. 2(h). Its amplitude increases when spots are closer to the zeroth diffraction order of the SLM. It originates from the SLM imperfections, namely the limited number of pixels and the crosstalk between neighboring pixels, which become particularly important at the positions corresponding to  $2\pi$  phase jumps between two consecutive pixels of the corrected phase mask. Note that aberration compensation also reduces the intensity of the background as seen by comparing fig. 3(d) and (h). This background significantly contributes to the distortion in shape and position of the individual spots. This is especially visible on the right side of arrays [Fig. 3(d)] where we observe a larger ellipticity of spots with random orientation.

## V. ARRAY OF BOTTLE BEAMS

We now apply our field compensation method to arrays of Bottle Beams (BOBs). These arrays are particularly valuable for optically trapping Rydberg atoms, which are low-field seekers[48, 49]. Similar BOBs, corrected using our method, have been used in[49] to trap Rydberg atoms over millisecond timescales. We prepare BOB arrays by adding a mask  $\phi_{\text{BOB}}(\rho)$  to the masks that generate the arrays of Gaussian spots. This added mask comprises two concentric areas with uniform phase and a  $\pi$  relative phase-shift. For the same pupil and Gaussian beam waist on the SLM as above, the central region's radius is set to approximately 3.35 mm in order to transform every Gaussian spot into a BOB, precisely centered at the same position.

Without field correction [fig.6(a)], BOBs, which are much more sensitive to aberrations than Gaussian spots, open even at the minimal distance of 18  $\mu\text{m}$  from the optical axis. At the array's periphery, the BOB's characteristic ring shape vanishes entirely, leaving only simple spots. In contrast, with field correction [fig.6(b)], all sites display the shape of a closed circle.

## VI. CONCLUSION

We have introduced a new method for the production of aberration-free arrays of focal points. It uses holographic masks generated by a phase-only SLM. Known adaptive optics methods compensate aberrations only close to a corrected spot, over a surface limited by the native FOV of the optical system. Our method, however, compensates the full accessible optical field. In addition, it is not limited to the generation of arrays of Gaussian tweezers. It produces high quality bottle beams, in spite of their critical sensitivity to aberrations. This is instrumental for the trapping of Rydberg atoms[48, 49]. The method can be used for generating arrays of arbitrarily shaped spots. It can also directly

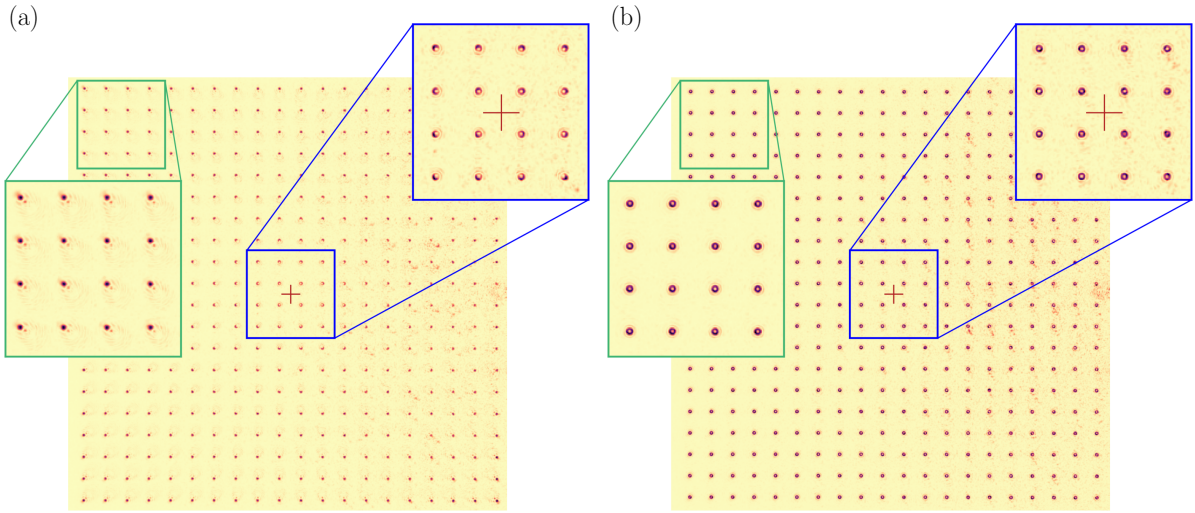


Figure 6. Field correction of a  $20 \times 20$  array of BOBs with  $d = 25 \mu\text{m}$ . The array covers a field of  $475 \times 475 \mu\text{m}$ . (a) and (b) are obtained without and with field correction respectively. In both cases, the mask  $\phi_0(\rho)$  is applied, correcting aberrations on the optical axis. Insets are zooms onto the central and top-left regions highlighted in blue and green, respectively. The red cross corresponds to the optical axis.

improve the quality of images obtained by scanning confocal microscopy[5, 29, 50], or sub-wavelength Scanning Near-field Optical Microscopy (SNOM)[51]. The method could be extended to the projection of arbitrary images instead of arrays of spots. This goes beyond the scope of this paper and will be the object of further studies.

As an illustration, we have applied our method to large-field aberration compensation of a low-cost aspherical lens, used out of its design wavelength range and presenting large imperfections. We have efficiently corrected the aberrations, extending its field of view from approximately  $50 \mu\text{m}$  to more than  $500 \mu\text{m}$ . The corrected field is only limited by the maximum accessible diffraction angle with our SLM and can be straightforwardly expanded by using an SLM with a larger number of pixels. This performance, obtained using a single aspherical lens, is comparable to state-of-the-art performances of complex, bulky, high-numerical-aperture objectives[24]. The method is essentially limited by the SLM imperfections creating a background speckle, which interfere with individual spots and induces fluctuations of the shapes (amplitude and ellipticity) and positions of spots. Higher quality SLMs with less crosstalk between pixels would considerably reduce the background speckle. Alternatively, the speckle can be made negligible using high-resolution lithographically-fabricated holograms.

The implementation of our aberration compensation method relies on the determination of only four generalized Seidel coefficients corresponding to coma of order 1 and 2, astigmatism and curvature and the centers of the latter two. These coefficients are determined by optical

measurements performed at a small number of reference points exploring the field of view of interest. The knowledge of these coefficients enables the generation of arbitrary arrays with a large number of spots. The method also applies to higher-order aberrations, corresponding to higher-order Zernike polynomials. Note that the method can also be used to generate 3D arrays of spots[21, 43, 52].

Finally, our method applies as well to any high-numerical-aperture optics with an optimized native large field in order to compensate for residual aberrations and further increase the aberration-compensated field of view. Our method thus drastically improves the useful field of any optical system used for generating large arrays of spots with foreseeable technological applications to high resolution imaging in biology by confocal microscopy, parallel laser machining of materials and 3D printing with optical resolution.

**Note added:** During the redaction of this manuscript, we became aware of related work also demonstrating full-field aberration compensation with a similar method[53].

This publication has received funding by the France 2030 programs of the French National Research Agency (Grant No. ANR-22-PETQ-0004, project QuBitAF), under Horizon Europe programme HORIZON-CL4-2022-QUANTUM-02-SGA via the project 101113690 (PASQuanS2.1), by the European Union (ERC Advanced Grant No. 786919, project TRENSCRYBE). It has been supported by the Quantum Information Center Sorbonne as part of the program *Investissements d'excellence* – IDEX of the Alliance Sorbonne Université.

[1] M. Born and E. Wolf, *Principles of Optics: Electromagnetic Theory of Propagation, Interference and Diffraction of Light* (Pergamon, Oxford, 1993).

[2] M. J. Booth, Adaptive optical microscopy: The ongoing quest for a perfect image, *Light: Science & Applications* **3**, e165 (2014).

[3] G. Zheng, X. Ou, R. Horstmeyer, and C. Yang, Characterization of spatially varying aberrations for wide field-of-view microscopy, *Optics Express* **21**, 15131 (2013).

[4] J. Nilsson, M. Evander, B. Hammarström, and T. Laurell, Review of cell and particle trapping in microfluidic systems, *Analytica Chimica Acta* **649**, 141 (2009).

[5] L. Schermelleh, R. Heintzmann, and H. Leonhardt, A guide to super-resolution fluorescence microscopy, *Journal of Cell Biology* **190**, 165 (2010).

[6] K. Dholakia and T. Čižmár, Shaping the future of manipulation, *Nature Photonics* **5**, 335 (2011).

[7] J. Wu, N. Ji, and K. K. Tsia, Speed scaling in multiphoton fluorescence microscopy, *Nature Photonics* **15**, 800 (2021).

[8] Y. Yang, Y.-X. Ren, M. Chen, Y. Arita, and C. Rosales-Guzmán, Optical trapping with structured light: A review, *Advanced Photonics* **3**, 10.1117/1.AP.3.3.034001 (2021).

[9] S. Hasegawa and Y. Hayasaki, Adaptive optimization of a hologram in holographic femtosecond laser processing system, *Optics Letters* **34**, 22 (2009).

[10] S. Hasegawa, H. Ito, H. Toyoda, and Y. Hayasaki, Massively parallel femtosecond laser processing, *Optics Express* **24**, 18513 (2016).

[11] H. Zhang, S. Hasegawa, H. Takahashi, H. Toyoda, and Y. Hayasaki, In-system optimization of a hologram for high-stability parallel laser processing, *Optics Letters* **45**, 3344 (2020).

[12] X. Wang, H. Yu, P. Li, Y. Zhang, Y. Wen, Y. Qiu, Z. Liu, Y. Li, and L. Liu, Femtosecond laser-based processing methods and their applications in optical device manufacturing: A review, *Optics & Laser Technology* **135**, 106687 (2021).

[13] N. Kuroo, F. Ishita, and Y. Hayasaki, Holographic laser processing with axial beam shaping optimized in optical system, *Optics Continuum* **4**, 1610 (2025).

[14] C. Mauclair, B. Najih, V. Comte, F. Bourquard, and M. Delaigue, Dynamic spatial beam shaping for ultrafast laser processing: A review, *Opto-Electronic Science* **4**, 250002 (2025).

[15] D. G. Grier, A revolution in optical manipulation, *Nature* **424**, 810 (2003).

[16] S. Bianchi and R. Di Leonardo, Real-time optical manipulation using optimized holograms generated on the GPU, *Computer Physics Communications* **181**, 1444 (2010).

[17] A. Jesacher and M. J. Booth, Parallel direct laser writing in three dimensions with spatially dependent aberration correction, *Optics Express* **18**, 21090 (2010).

[18] L. Zhang, C. Wang, C. Zhang, Y. Xue, Z. Ye, L. Xu, Y. Hu, J. Li, J. Chu, and D. Wu, High-Throughput Two-Photon 3D Printing Enabled by Holographic Multi-Foci High-Speed Scanning, *Nano Letters* **24**, 2671 (2024).

[19] P. Somers, A. Münchinger, S. Maruo, C. Moser, X. Xu, and M. Wegener, The physics of 3D printing with light, *Nature Reviews Physics* **6**, 99 (2024).

[20] F. Nogrette, H. Labuhn, S. Ravets, D. Barredo, L. Béguin, A. Vernier, T. Lahaye, and A. Browaeys, Single-Atom Trapping in Holographic 2D Arrays of Microtraps with Arbitrary Geometries, *Phys. Rev. X* **4**, 021034 (2014).

[21] D. Barredo, V. Lienhard, S. de Léséleuc, T. Lahaye, and A. Browaeys, Synthetic three-dimensional atomic structures assembled atom by atom, *Nature* **561**, 79 (2018).

[22] D. Kim, A. Keesling, A. Omran, H. Levine, H. Bernien, M. Greiner, M. D. Lukin, and D. R. Englund, Large-scale uniform optical focus array generation with a phase spatial light modulator, *Optics Letters* **44**, 3178 (2019).

[23] K.-N. Schymik, B. Ximenez, E. Bloch, D. Dreon, A. Signoles, F. Nogrette, D. Barredo, A. Browaeys, and T. Lahaye, In situ equalization of single-atom loading in large-scale optical tweezer arrays, *Physical Review A* **106**, 022611 (2022).

[24] H. J. Manetsch, G. Nomura, E. Bataille, X. Lv, K. H. Leung, and M. Endres, A tweezer array with 6100 highly coherent atomic qubits, *Nature* **1** (2025).

[25] G. Pichard, D. Lim, É. Bloch, J. Vaneechloo, L. Bourachot, G.-J. Both, G. Mériaux, S. Dutartre, R. Hostein, J. Paris, B. Ximenez, A. Signoles, A. Browaeys, T. Lahaye, and D. Dreon, Rearrangement of individual atoms in a 2000-site optical-tweezer array at cryogenic temperatures, *Physical Review Applied* **22**, 024073 (2024).

[26] N.-C. Chiu, E. C. Trapp, J. Guo, M. H. Abobeih, L. M. Stewart, S. Hollerith, P. L. Stroganov, M. Kalinowski, A. A. Geim, S. J. Evered, S. H. Li, X. Lyu, L. M. Peters, D. Bluvstein, T. T. Wang, M. Greiner, V. Vuletić, and M. D. Lukin, Continuous operation of a coherent 3,000-qubit system, *Nature* **10.1038/s41586-025-09596-6** (2025).

[27] R. Lin, H.-S. Zhong, Y. Li, Z.-R. Zhao, L.-T. Zheng, T.-R. Hu, H.-M. Wu, Z. Wu, W.-J. Ma, Y. Gao, Y.-K. Zhu, Z.-F. Su, W.-L. Ouyang, Y.-C. Zhang, J. Rui, M.-C. Chen, C.-Y. Lu, and J.-W. Pan, AI-Enabled Parallel Assembly of Thousands of Defect-Free Neutral Atom Arrays, *Physical Review Letters* **135**, 060602 (2025).

[28] H. W. Babcock, THE POSSIBILITY OF COMPENSATING ASTRONOMICAL SEEING, *Publications of the Astronomical Society of the Pacific* **65**, 229 (1953).

[29] M. J. Booth, M. A. A. Neil, R. Juškaitis, and T. Wilson, Adaptive aberration correction in a confocal microscope, *Proceedings of the National Academy of Sciences of the United States of America* **99**, 5788 (2002).

[30] R. Davies and M. Kasper, Adaptive Optics for Astronomy, *Annual Review of Astronomy and Astrophysics* **50**, 305 (2012).

[31] P. S. Salter and M. J. Booth, Adaptive optics in laser processing, *Light: Science & Applications* **8**, 110 (2019).

[32] D. L. Fried, Anisoplanatism in adaptive optics, *JOSA* **72**, 52 (1982).

[33] R. D. Simmonds and M. J. Booth, Modelling of multi-conjugate adaptive optics for spatially variant aberrations in microscopy, *Journal of Optics* **15**, 094010 (2013).

[34] J. Mertz, H. Paudel, and T. G. Bifano, Field of view advantage of conjugate adaptive optics in microscopy applications, *Applied Optics* **54**, 3498 (2015).

[35] F. Rigaut and B. Neichel, Multiconjugate Adaptive Optics for Astronomy, *Annual Review of Astronomy and Astrophysics* **56**, 277 (2018).

[36] Y. Machu, C. Sayrin, and M. Brune, *Patent FR2315493*.

[37] Y. Machu, *Mesure non destructive et manipulation locales d'atomes de Rydberg circulaires en pinces optiques*, Ph.D. thesis, Sorbonne Université (2024).

[38] *See Supplementary Material.*

[39] J. Arlt and M. J. Padgett, Generation of a beam with a dark focus surrounded by regions of higher intensity:

The optical bottle beam, *Optics Letters* **25**, 191 (2000).

[40] S. Zhang, F. Robicheaux, and M. Saffman, Magic-wavelength optical traps for Rydberg atoms, *Phys. Rev. A* **84**, 043408 (2011).

[41] Hamamatsu X13138-03.

[42] R. Gerchberg, A practical algorithm for the determination of phase from image and diffraction plane pictures, *Optik* (1972).

[43] R. D. Leonardo, F. Ianni, and G. Ruocco, Computer generation of optimal holograms for optical trap arrays, *Optics Express* **15**, 1913 (2007).

[44] B. M. Hanser, M. G. L. Gustafsson, D. A. Agard, and J. W. Sedat, Phase retrieval for high-numerical-aperture optical systems, *Optics Letters* **28**, 801 (2003).

[45] G. Conforti, Zernike aberration coefficients from Seidel and higher-order power-series coefficients, *Optics Letters* **8**, 407 (1983).

[46] V. Lakshminarayanan and A. Fleck, Zernike polynomials: A guide, *Journal of Modern Optics* **58**, 545 (2011).

[47] *OSLO, Optics Software for Layout and Optimization* (Lambda Research Corporation).

[48] D. Barredo, V. Lienhard, P. Scholl, S. de Léséleuc, T. Boulier, A. Browaeys, and T. Lahaye, Three-Dimensional Trapping of Individual Rydberg Atoms in Ponderomotive Bottle Beam Traps, *Physical Review Letters* **124**, 023201 (2020).

[49] B. Ravon, P. Méhaignerie, Y. Machu, A. D. Hernández, M. Favier, J. M. Raimond, M. Brune, and C. Sayrin, Array of Individual Circular Rydberg Atoms Trapped in Optical Tweezers, *Physical Review Letters* **131**, 093401 (2023).

[50] F. Helmchen and W. Denk, Deep tissue two-photon microscopy, *Nature Methods* **2**, 932 (2005).

[51] S. W. Hell and J. Wichmann, Breaking the diffraction resolution limit by stimulated emission: Stimulated-emission-depletion fluorescence microscopy, *Optics Letters* **19**, 780 (1994).

[52] W. Lee, H. Kim, and J. Ahn, Three-dimensional rearrangement of single atoms using actively controlled optical microtraps, *Optics Express* **24**, 9816 (2016).

[53] I. Christen, C. Panuski, T. Propson, and D. Englund, Full-volume aberration-space holography (2025), arXiv:2505.08777 [physics].